electronics

MDPI

Article

Introduction of a Novel Image-Based and Non-Invasive Method for the Estimation of Local Elastic Properties of Great Vessels

Benigno Marco Fanni [1,*,†], Alessandra Pizzuto [2], Giuseppe Santoro [2] and Simona Celi [1,*,†]

[1] BioCardioLab, Bioengineering Unit, Fondazione Toscana "G. Monasterio", 54100 Massa, Italy
[2] Pediatric Cardiology Unit, Fondazione Toscana "G. Monasterio", 54100 Massa, Italy; apizzuto@ftgm.it (A.P.); gsantoro@ftgm.it (G.S.)
* Correspondence: bmfanni@ftgm.it (B.M.F.); s.celi@ftgm.it (S.C.)
† These authors contributed equally to this work.

Abstract: Background: In the context of a growing demand for the use of in silico models to meet clinical requests, image-based methods play a crucial role. In this study, we present a parametric equation able to estimate the elasticity of vessel walls, non-invasively and indirectly, from information uniquely retrievable from imaging. Methods: A custom equation was iteratively refined and tuned from the simulations of a wide range of different vessel models, leading to the definition of an indirect method able to estimate the elastic modulus *E* of a vessel wall. To test the effectiveness of the predictive capability to infer the *E* value, two models with increasing complexity were used: a U-shaped vessel and a patient-specific aorta. Results: The original formulation was demonstrated to deviate from the ground truth, with a difference of 89.6%. However, the adoption of our proposed equation was found to significantly increase the reliability of the estimated E value for a vessel wall, with a mean percentage error of 9.3% with respect to the reference values. Conclusion: This study provides a strong basis for the definition of a method able to estimate local mechanical information of vessels from data easily retrievable from imaging, thus potentially increasing the reliability of in silico cardiovascular models.

Keywords: vascular modeling; imaging; fluid-structure interaction; computational fluid dynamics; numerical models; mechanical properties; MRI

Citation: Fanni, B.M.; Pizzuto, A.; Santoro, G.; Celi, S. Introduction of a Novel Image-Based and Non-Invasive Method for the Estimation of Local Elastic Properties of Great Vessels. *Electronics* **2022**, *11*, 2055. https://doi.org/10.3390/electronics11132055

Academic Editor: Yu Zhang

Received: 6 May 2022
Accepted: 25 June 2022
Published: 30 June 2022

1. Introduction

Over recent decades, the use of patient-specific numerical models has continued to grow for an increasing range of applications [1–3]. Recent technological advances in medical imaging and computational power have enabled the increased use of numerical patient-specific modeling, providing a reliable tool for the study of cardiovascular problems in a highly accurate way.

The use of computer-based models has been strongly encouraged for in silico clinical trials, as advocated by the FDA (Food and Drug Administration) to enable the development of new devices and therapeutic applications [4]. Moreover, these models represent a powerful and promising tool for the pre-procedural assessment of cardiovascular interventions during the decision-making process [5].

However, the translation of numerical modeling into effective clinical applications is still limited, as the reliable adaption of cardiovascular models for patient-specific conditions represents a major challenge [6–8]. The current imaging techniques allow a high-fidelity depiction of in vivo anatomical structures of the patient, and structural 3D-imaging methods, such as computed tomography (CT) and magnetic resonance imaging (MRI) are commonly used worldwide. However, a proper numerical replica of the patient's case requires faithful implementation of boundary conditions and material properties, with the latter currently representing the biggest source of uncertainty [9,10]. However, functional

imaging methodologies, such as phase contrast MRI, 4D flow and Doppler ultrasound, can provide useful and detailed in vivo information on the patient's hemodynamics, allowing for the implementation of accurate boundary conditions [11–13],when patient-specific material characteristics remain unknown.

The lack of such crucial information results in approximations in material modeling [14–16], thus strongly limiting the reliability of numerical tools. The mechanical response of vessels, as a result of blood flowing [17,18] or device interaction [19], depends not only on the material properties of the vessel itself, but also on the surrounding structures and tissues [20], thus, in some cases, reducing the value of ex vivo data [21]. Given the importance of non-invasively extrapolating in vivo material information relating to cardiovascular structures, several approaches have been investigated over recent years, such as inverse numerical methodologies and image-based techniques [22–24]. The high computational cost of iterative methods strongly limits their practical use in clinics, where prompt feedback is necessary. However, actual image-based strategies for inferring mechanical properties are limited to the use of pressure information [25,26], which is not only invasive but is also not always available for patients. Among such methodologies, elastography represents a non-invasive imaging technique for the quantitative assessment of tissue elasticity [27–29]. However, despite its increasing clinical relevance, especially in non-vascular areas [27], vascular elastography was demonstrated to detect statistically significant elasticity differences in patient tissues, and was thus able to distinguish different plaque types with acceptable reproducibility [30], but without providing exact absolute stiffness values for vessel structures in a way that can be implemented in numerical models.

Such strategies highlight the importance of image-based methods, which are now crucial elements of clinical workflow [31,32], to be considered for the estimation of the material characteristics of in vivo vessel walls. Enhanced material information, which includes in vivo patient-specific data, may significantly improve the accuracy of computational models, increasing their validity and applicability in clinical practice.

In this study, we develop a non-invasive image-based methodology able to infer the local elastic modulus of arterial walls at specific sections of the vessels, without using pressure invasive information. The unique requirements of the proposed method are dynamic information of area deformation and flow measurements along the cardiac cycle, which are both easily retrievable from standard functional imaging, such as phase contrast MRI, which is a routine examination in the pre-procedural assessment of the patient before scheduled cardiovascular intervention. The method described here is based on our previous results [33], where a new formulation was introduced. In this study, we generalize its application to a wide range of vessels, enabling the estimation of patient-specific material information from solely in vivo MRI data. The methodology was refined based on a series of numerical simulations, enabling the exploration of a huge number of vascular geometries and fluid dynamics scenarios in a fully controlled in silico environment. In particular, each numerical vessel was treated as a virtual patient, from which virtual phase contrast MRI information was acquired at specific cross-sections, in terms of velocity variation and area deformation along the simulated cardiac cycle, thus permitting the application of the QA method and consequent PWV and E value estimation. After finalizing its mathematical formulation, the presented technique was tested on two virtual datasets generated from computer simulations with increased complexity, thus demonstrating its efficacy.

2. Materials and Methods

2.1. Theoretical Background

The so-called flow-area (QA) method is an image-based technique which enables the calculation of the local pulse wave velocity (PWV) [34] of a vessel from through-plane flow and cross-sectional area as extracted from imaging, such as phase contrast MRI [35] or Doppler ultrasound [36]. The PWV is a widely accepted parameter for the estimation of arterial stiffness in clinics [37–39].

The QA methodology is based on the assumption that, during the reflection-free period of the cardiac cycle, i.e., the early systolic phase, the relationship between the cross-sectional area A of the vessel and the passing flow Q can be approximated as a first-order linear equation, allowing the estimation of the PWV as:

$$PWV = \left.\frac{dQ}{dA}\right|_{\text{early systole}} \tag{1}$$

where dA is the incremental variation of the cross-sectional area and dQ is the incremental variation of the flow passing through the section. A representation of the steps for the computing of the PWV from phase contrast MRI data is depicted in Figure 1.

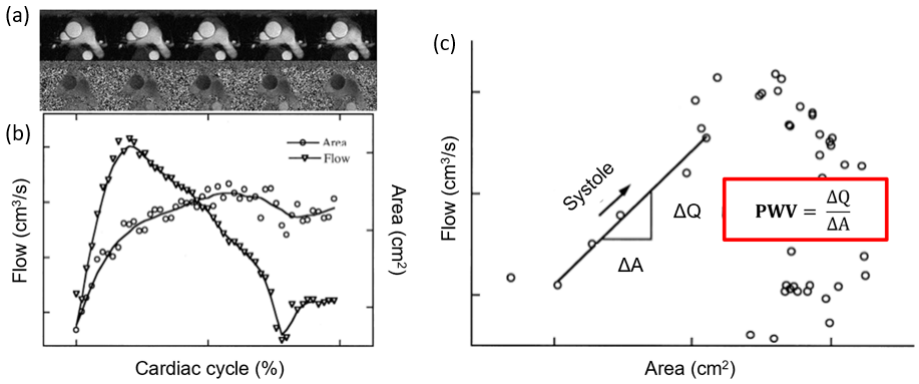

Figure 1. (**a**) Phase contrast images of an aortic section; (**b**) Through plane flow Q and area A variations along the cardiac cycle as extracted from phase contrast data segmentation; (**c**) QA loop for the estimation of the PWV as the slope of the early-systole period.

The PWV can be used as a starting point for the estimation of additional parameters providing further information on the mechanical response of an in vivo vessel wall.

By inverting the well-known Bramwell–Hill equation [40], the distensibility ($Dist$) of a vessel can be defined from the PWV:

$$Dist = \frac{1}{\rho\, PWV^2} \tag{2}$$

where ρ is the density of the fluid passing through the cross-section of the vessel, i.e., the blood density in vascular structures.

Finally, according to [41], an estimation of the elastic modulus E of the vessel wall can be expressed as a function of the $Dist$ and some geometrical features of the vessel:

$$E_{Dist} = \frac{\left[3\left(1+\frac{A_0}{WCSA}\right)\right]}{Dist} \tag{3}$$

in which A_0 is the diastolic inner area of the vessel and $WCSA$ is the wall cross-sectional area (i.e., the area between the inner and outer diameter), also measured at diastole, expressed as:

$$WCSA = \pi(r_0 + thk)^2 - \pi r_0^2 \tag{4}$$

where r_0 represents the inner diastolic radius of the vessel and thk is the wall thickness.

By combining Equations (1) and (3), a PWV-based E value of the vessel wall can be therefore defined as:

$$E_{PWV} = 3\,\rho\, PWV^2\left(1+\frac{A_0}{WCSA}\right) \tag{5}$$

where the PWV can be obtained from the QA method using Equation (1). Hence, Equation (5) can be used to estimate a surrogate of the E value of a vessel wall from solely image-based information.

In the following, an improved version of Equation (5) is presented, obtained from a recursive in silico method based on FSI simulations.

2.2. Definition of the Image-Based Formulation

In this section, the image-based formulation for the estimation of the E value of vessel walls is described. The starting point was represented by the Equation (5), based on PWV and other parameters. First, the aforementioned formulation was tested to assess its capability to predict the E value of a vessel wall. In particular, an in silico workflow based on a series of FSI simulations of vessels models was developed. FSI results of vessel models were treated as super-resolution phase contrast MRI datasets, with the advantage of an absence of noise and artifacts with respect to real imaging. Hence, flow and area information were extracted for each simulated model from a single cross-section, as occurs in proper image data, to compute PWV and then the E value from Equation (5). For each simulated vessel, the outcome from Equation (5) was compared to the E value assigned to the in silico model. Since a discrepancy was observed between E estimation and the ground truth, a correction factor was included in the formula and iteratively calibrated to reduce the error.

Following the preliminary results from [33], the correction factor (χ) was defined as:

$$\chi = \gamma\, RAC \tag{6}$$

where RAC is the relative area change in the cardiac cycle, expressed as:

$$RAC = \frac{A_{\max} - A_0}{A_{\max}} \tag{7}$$

in which A_{max} is the maximum cross-sectional area of the vessel lumen, i.e., the area value at systolic peak, and A_0 is the area value at diastole. The parameter γ was assumed as a function of some model characteristics, such as geometry, flow and pressure quantities, as detailed in the following.

The inclusion of the χ factor (Equation (6)) in the formulation was demonstrated to increase its predictive capability in the estimation of the E value of the vessel wall [33]. Briefly, the enhanced formula for the estimation of the E value is provided by multiplying the Equations (5) and (6):

$$E_\chi = 3\,\chi\,\rho\, PWV^2 \left(1 + \frac{A_0}{WCSA}\right) \tag{8}$$

The χ-method is able to estimate the local E value of a vessel wall at a selected cross-section, using the Equation (1), which considers the PWV as computed from the QA method, specific geometric features of the section, and a crucial corrective factor χ.

The original formulation (Equation (5)) was used to indirectly compute the E value, which was compared to the E value assigned as input in the numerical model. Due to the non-linearity observed between input and output E values, the corrective factor χ (Equation (6)) was introduced to reduce such non-linearity and increase the goodness of the estimation.

While in the previous study, γ was computed for a single configuration, here, in order to generalize its formulation, we defined the variable γ as a function of three main parameters: the cross-sectional area of the vessel at diastole (A^d), the peak of the passing through-plane flow (Q^p) and the internal pressure range (P):

$$\gamma = \Gamma(A^d, Q^p, P) \tag{9}$$

Solving the problem for two principal pressure configurations, the P range can be assumed to be equal to 80–120 mmHg in the case of aortic pressure (P_{Ao}) or 10–22 mmHg in the case of pulmonary artery pressure (P_{PA}). These ranges were selected to cover the cases of the two main great vessels pressure ranges. Hence, Equation (10) becomes:

$$\gamma|_{P_{Ao}} = \Gamma(A^d, Q^p, P = P_{Ao}) \quad \text{and} \quad \gamma|_{P_{PA}} = \Gamma(A^d, Q^p, P = P_{PA}) \tag{10}$$

To investigate the influence of A^d and Q^p values on γ, five pipe vessels with inner diameters (D) equal to 1, 2, 3, 4 and 5 cm were modeled, corresponding to human vessel common sizes (Table 1). The length and wall thickness of vascular models were maintained constant, i.e., 15 cm and 0.2 cm, respectively.

Table 1. List of parameters used for the FSI simulations.

A_i^d (cm^2)	Q_j^p (mL/s)	E_k^w (MPa)
0.78	100	0.5
3.14	200	1.0
7.07	300	2.0
12.57	400	4.0
19.64	500	8.0

For the i-th geometry characterized by a diastolic cross-sectional area A_i^d, five different inflow velocity boundary conditions were adopted, so that five flow peaks Q^p were considered, ranging from 100 to 500 mL/s (Table 1). The outflow pressure boundary condition was imposed according to the two main pressure ranges P_{Ao} and P_{PA}.

Then, for each model characterized by the i-th geometry and the j-th inflow boundary condition (A_i^d and Q_j^p, respectively), five simulations with increasing elastic modulus assigned to the vessel wall (E^w), in the range 0.5–8 MPa (Table 1), were run.

The value of $\gamma_{i,j}$ for the vessel model characterized by a diastolic area A_i^d and a flow peak of Q_j^p at the selected section, and an internal pressure range P_0 (P_{Ao} or P_{PA} in this study) is estimated as:

$$\gamma_{i,j} = \Gamma(A_i^d, Q_j^p, P_0) = \sum_{k=1}^{n} \frac{\psi_k}{n} \tag{11}$$

with ψ_k computed as follows:

$$\psi_k = \frac{E_k^w}{RAC(A_i^d)\, E_{PWV}(A_i^d, Q_j^p)} \tag{12}$$

where E_k^w is the k-th elastic modulus assigned to the vessel wall in the simulation, RAC is the relative area change of the model (Equation (7)), which is a function of the cross-sectional area A_i^d, and E_{PWV} is the E value as obtained from standard Equation (5), dependent on both the diastolic area A_i^d and the flow peak Q_j^p for the calculation of PWV (Equation (1)) and the geometric features. Parameters A_i^d, Q_j^p and E_k^w are listed in Table 1.

Each simulation, characterized by a diastolic area A_i^d, a flow peak Q_j^p and an elastic modulus for the vessel wall E_k^w, was run twice, first with an outflow pressure condition P_{Ao} and then with P_{PA}, while inflow boundary condition was maintained.

The two obtained datasets were interpolated using the thin-plate spline for surfaces using MATLAB (MathWorks, Inc., Natick, MA, USA), to obtain a complete estimation of $\gamma|_{Ao}$ and $\gamma|_{PA}$ domains.

Due to the huge amount of simulations required to characterize the γ domain, a custom-made pipeline was developed in Python to automatize all the steps of the process in an optimized manner, from the set-up of the simulations to the elaboration of the results.

2.3. Fluid-Structure Interaction Simulation Workflow

The numerical simulations were carried out with the commercial software LS-DYNA R.11 (Ansys/LST, Ansys Inc., Canonsburg, PA, USA). In order to simulate pulsatile cardiac-like flow within the different compliant virtual vessel models, a two-way approach with a strong coupling scheme was adopted to encompass the influence of the passing flow on the deformable structure of the vessel wall and the reciprocal effect. An arbitrary Lagrangian Eulerian formulation was used for the mesh deformation. Both fluid and solid discrete systems were considered as converged when their respective residuals dropped below threshold $\epsilon = 1 \times 10^{-6}$ at every time step. Fluid and structural domains had matching interfaces for an optimal solution exchange.

In silico models. The FSI simulations were run for a set of vessel pipe models with cylindrical shape, and used to estimate the γ domain, as described in Section 2.2. The model sets included a total of five different cylindrical geometries, with inner diameters (D), according to Table 1.

Fluid domains. The unsteady fluid computation analysis of the FSI models was performed using the ICFD solver of LS-DYNA. The fluid behavior is governed by the Navier–Stokes equations, with the ICFD solver discretizing the governing equations using a low-order continuous finite element method. The models were meshed with tetrahedral elements using the commercial package ANSA (BETA CAE Systems International AG, Luzern, Switzerland), using an average element size of 1 mm. A preliminary mesh convergence study was performed to confirm a mesh-independent solution. The blood behaviour was simulated as an incompressible and Newtonian fluid with a density of 1060 kg m^3 and a dynamic viscosity of 0.05 kg m^{-1} s^{-1}. The boundary conditions were implemented to impose idealised, but physically based, waveforms of cardiac-like velocities at the inlet and pressures at the outlet. In particular, boundary conditions for the five pipe models are shown in Figure 2, with reference to the different Q^p for the inlet (Figure 2a) and the two analyzed pressure conditions (P_{Ao} and P_{PA}) for the outlet (Figure 2b).

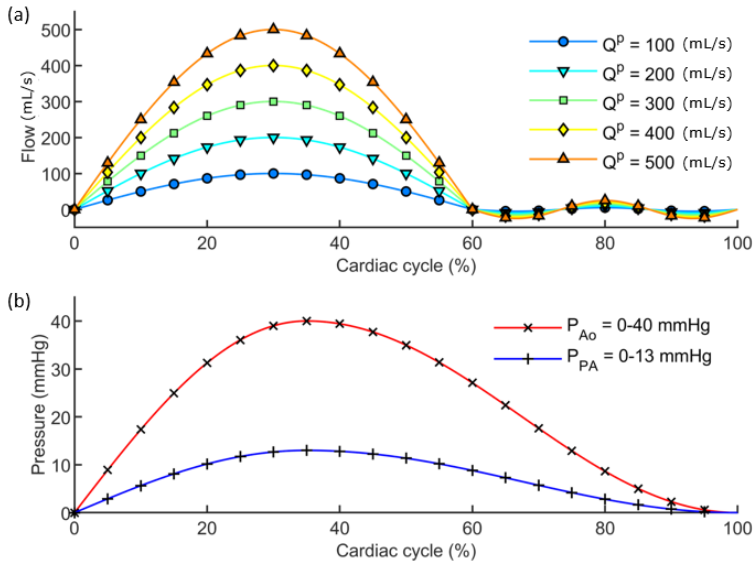

Figure 2. (**a**) Inflow boundary conditions related to the five flow peak Q^p values implemented; (**b**) Outflow boundary conditions related to the two implemented pressure ranges (P_{Ao} and P_{PA}).

Structural domains. Structural models consisted of the solid walls of the FSI models. In all cases a constant wall thickness of 2 mm was set. A node-to-node correspondence between the fluid and solid parts was accomplished by the ANSA meshing software. The governing equations for the structural domain are those of linear elasticity for small deformations, discretized by the solver with a continuous finite element method. Material was modeled as isotropic linear elastic, with a Poisson ratio of 0.49. A range of different E values was

assigned to the models. The different values of stiffness were set according to Table 1. The structural models were bounded with fixed edges.

Post-processing of simulations. The post-processing of the run models was handled in ParaView (www.paraview.org, accessed on 28 March 2022) [42] and MATLAB. Results from the FSI simulations were exported in *.vtk* format to be elaborated in ParaView. Treated as virtual patients, the results from the FSI models were analyzed at a selected cross-section (S), as happens during real phase contrast MRI acquisitions. In particular, the results from pipe vessel models were analyzed at the middle cross-section of the cylindrical models, to avoid edge effects. Area deformation and through-plane flow over time were extracted for each case to define the related QA loop. Finally, the procedure described in the previous Section 2.2 was applied for the definition of the γ domain.

2.4. Application of the Image-Based Method to Virtual Models

The χ-method described in the previous sections was applied for validation purposes on two different models M_1 and M_2 consisting of two FSI models of increasing morphological complexity.

Geometries. The first model (M_1) consisted of a more complex version of the pipe vessels used to define the γ domain (Section 2.3), where the cylindrical shape was bent in a "U" configuration, thus representing an idealized model of an aortic arch (Figure 3a). The M_2 geometry was designed in the Fusion 360 environment (Autodesk, San Rafael, California). A U-shape presented a circular section characterized by a diameter of 2 cm. The straight tracts measured 10 cm, with a curvature radius of 3 cm in the bent region.

The second model (M_2) was of an actual patient-specific aorta, including ascending and descending tracts and supra-aortic vessels. The geometry of M_2 was extracted from the segmentation of patient CT imaging (Figure 4a) using the open source package 3D Slicer (Slicer, USA). A 2 mm thickness wall was set for both M_1 and M_2 models.

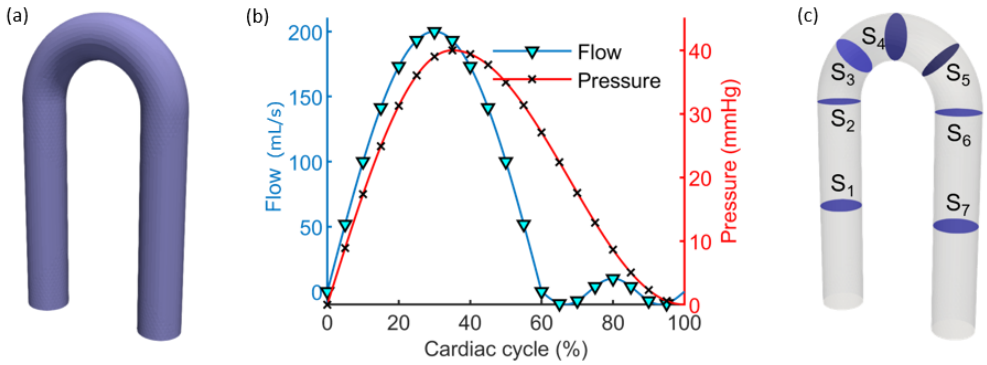

Figure 3. (**a**) Rendering of the U-shaped model; (**b**) Flow and pressure boundary conditions applied to the inlet and outlet of the U-shaped model; (**c**) Visualization of the seven cross-sections defined for the U-shaped model.

Materials. Material of the structural wall was modeled as isotropic linear elastic, with a Poisson ratio of 0.49. FSI simulations of M_1 and M_2 models were run with different E values for the vessel wall, from softer to harder values. In this testing phase, the a priori knowledge of the E values of M_1 and M_2 models permitted the availability of a reliable ground truth for the comparison with the E_χ values, as computed from Equation (8) including the corrective factor χ. However, the assigned stiffness values were different from the E values used to populate the γ domain (Section 2.2), to quantify the goodness of the obtained surface in regions out of the interpolation points. In particular, four E values were assigned, i.e., 1.5, 2.3, 2.7 and 3.0 MPa. The blood behaviour was simulated as an incompressible and non-Newtonian fluid with a density of 1060 kg m^3 and a dynamic viscosity of 0.05 kg m^{-1} s^{-1}.

Meshes. All fluid parts were meshed with tetrahedral elements using the commercial package ANSA The M_1 model was meshed with 82,803 elements. M_2 was meshed with 835,156 elements including four inflation layers with a growth rate of 1.5. Additional extrusions were added at the inlet of the model, and at the supra-aortic and descendent tracts, to allow the flow to fully develop. Structural meshes were defined with two layers among the thickness wall, imposing a node-to-node correspondence between domains. A preliminary mesh convergence study was performed to confirm a mesh-independent solution for the two models.

Boundary conditions. All the structural models were bounded with fixed edges. Concerning fluid domains, the boundary conditions were implemented to impose cardiac-like velocities at the inlet and pressures at the outlet.

M_2 was treated as a simplified aorta, thus modeled with the P_{Ao} outflow pressure condition and the flow curve equivalent to $Q_p = 200$ mL/s for the inlet condition (Figure 3b), with reference to Figure 2. Regarding M_2, a complete patient-specific model was implemented. The inlet condition was set according to flow measurements from phase contrast MRI of the patient at the aortic valve level (Figure 4b), while outlet conditions for the descending aorta and supra-aortic vessels were based on the Windkessel model [43], with RCR parameters set according to a previous study [1] in order to guarantee the pressure range of the patient (40 mmHg peak-to-peak) and a physiological waveform.

Solutions. A total of eight FSI simulations were run, considering the two models M_1 and M_2 and the four values of stiffness implemented for the walls (E_1 = 1.5 MPa, E_2 = 2.3 MPa, E_3 = 2.7 MPa, E_4 = 3.0 MPa). The solving was carried out in LS-DYNA and using the same solution parameters set in Section 2.3. Three cardiac cycles were simulated for M_1, and only the last cycle was considered for analysis. Instead, a total of ten cardiac cycles were simulated for M_2, allowing the *RCR* models to reach the regime state.

Post processing. Being treated as virtual patients, the results from the two FSI models were analyzed at selected cross-sections (S), as happens during phase MRI acquisitions.

Seven cross-sections were extracted from the FSI results of M_1, to capture the effect of straight and bent tracts on the analysis (Figure 3b). In particular, S_1 and S_7 originated from a cut-plane at 5 cm height from base. Similarly, a cut-plane at 10 cm height was used to select S_2 and S_6. Instead, S_3 and S_5 were derived from the cut-planes defined in the regions of maximum warp, for ascending and descending tracts, respectively, while S_4 was extracted from the plane of symmetry.

For the patient-specific case, M_2, the cut planes for the extraction of the slices were defined as perpendicular to the center line of the model. The open source library VMTK (Orobix srl, Bergamo, Italy) was used to compute the center line. Five slices were analyzed for M_2: on the aortic root (S_1), on the ascending tract (S_2), on the descending bend after the supra-aortic vessels (S_3), and on the descending tract at proximal (S_4) and distal positions (S_5), as depicted in Figure 4c.

For each slice S of each model, area deformation and through-plane flow along time were extracted. The QA method was applied to compute the PWV according to Equation (1). Then, E_χ at section S was calculated according to Equation (8), with γ value equal to:

$$\gamma_S = \Gamma(A_S^d, Q_S^p, P_0 = P_{Ao}), \tag{13}$$

where A_S^d and Q_S^p are the diastolic area and the flow peak measured at section S, and P_0 the known pressure range (P_{Ao} in these cases). The estimated E_χ value was compared with respect to the E value assigned as input to the numerical simulation to verify the efficacy of the χ-method. E_{PWV} was computed as well using Equation (5), to compare the standard methodology and the novel χ-method in terms of inferring the capability of the E value.

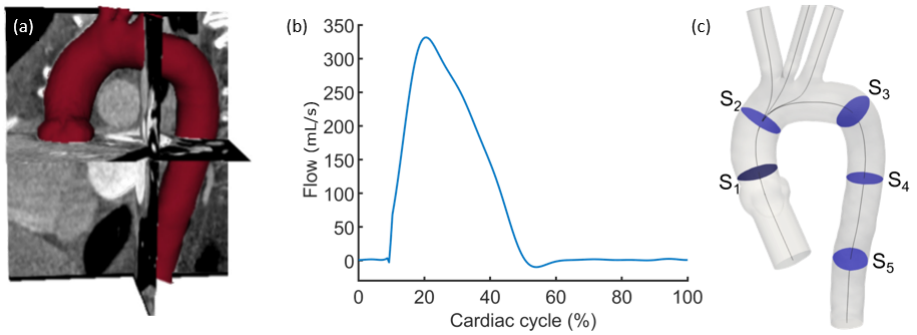

Figure 4. (**a**) Patient-specific aorta model segmentation from the CT dataset; (**b**) Flow boundary conditions applied to the inlet of the aortic model as extracted from patient phase contrast MRI data; (**c**) Visualization of the five cross-sections defined for the patient-specific model based on center line perpendicularity.

3. Results

3.1. Results from the Simulations Workflow

The definition of the γ function through the massive in silico campaign was achieved successfully. Figure 5 depicts the post-processing of an example case of an FSI simulation, from the selection of the middle cross-section of the model results to the computation of area and flow quantities along the cardiac cycle for the building of the QA loop.

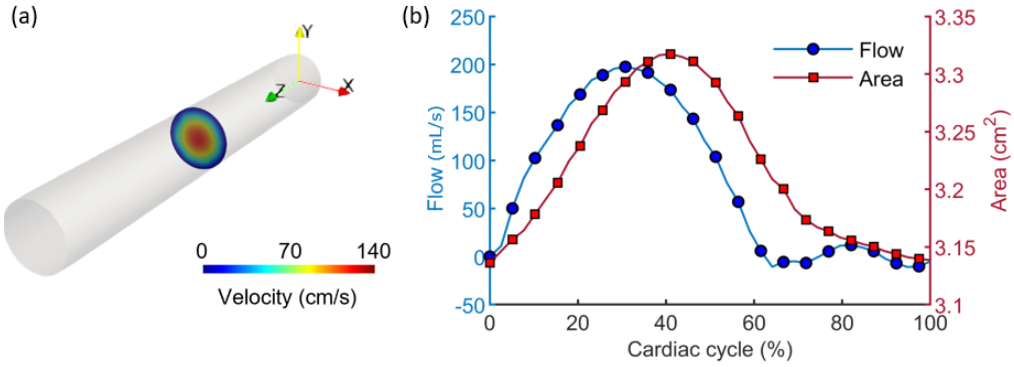

Figure 5. Extraction from the middle cross-section of the vascular model (**a**) of through-plane flow and area deformation along the cardiac cycle (**b**). This example is related to the FSI simulation with D^d = 2 cm, Q^p = 200 mL/s and E^w = 1 MPa.

The execution of the same procedure for all the run models allowed the population of the γ domain at selected (A, Q) points, based on the value listed in Table 1.

Figure 6 shows the trend of γ values (mean $\pm$ standard deviation) with respect to the diastolic inner diameter D^d (hence, inner diastolic area A^d) at constant flow (Figure 6a–c) and vice versa (Figure 6b–d), for the two analyzed pressure scenarios (i.e., P_{Ao} and P_{PA}). In particular, γ was found to increase with larger vessels and decrease with greater passing flow. Moreover, γ appeared to be specifically sensible to pressure variations, presenting higher values with higher pressures, as demonstrated by the difference between the graphs related to P_{Ao} and P_{PA}, respectively, reported in Figure 6a,b and Figure 6c,d.

In order to determine the effect of the mutual contribution of A and Q on the γ response, a 3D interpolation using a thin-plate spline for surfaces was performed. Figure 7 shows the results of the interpolation for $\gamma|_{Ao}$ and $\gamma|_{PA}$, respectively, depicted in Figure 7a and Figure 7b.

As can be seen in Figure 7a,b, a difference in the γ range between the two pressure scenarios was found. As expected, $\gamma|_{Ao}$ exhibited higher values with respect to the $\gamma|_{PA}$. However, their ratio $\gamma|_{Ao} : \gamma|_{PA}$ was relatively constant among the flow-area plane

(Figure 7c), except for the regions representing non-realistic conditions, as for vessels with significantly reduced lumen and high flows.

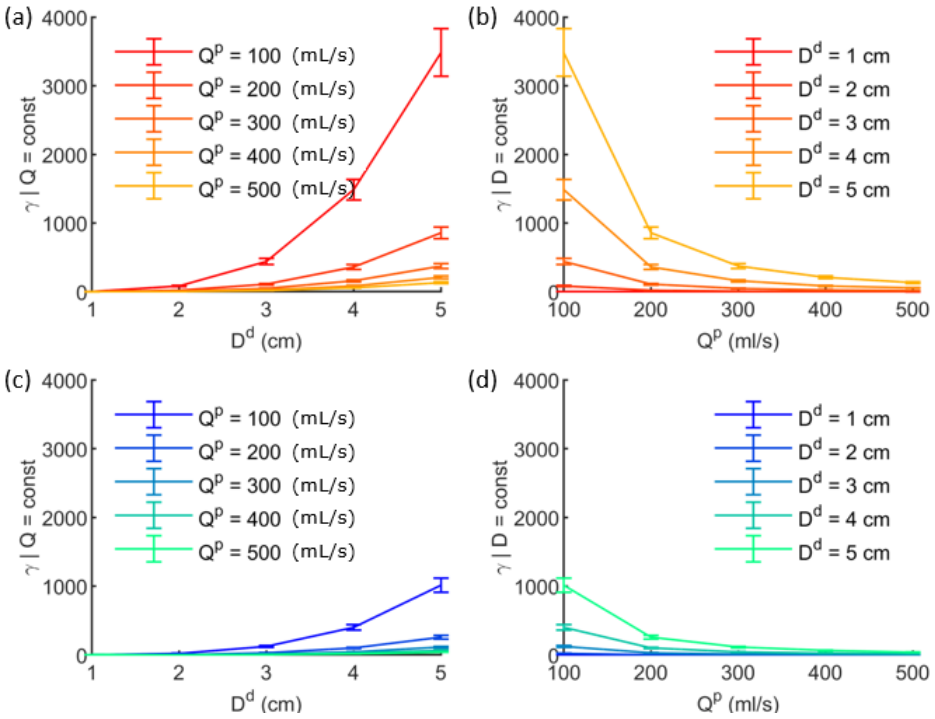

Figure 6. (**a**,**b**) Trend of $\gamma|_{Ao}$ with respect to diastolic diameter at constant flow (**a**) and vice versa (**b**); (**c**,**d**) Trend of $\gamma|_{PA}$ with respect to diastolic diameter at constant flow (**c**) and vice versa (**d**).

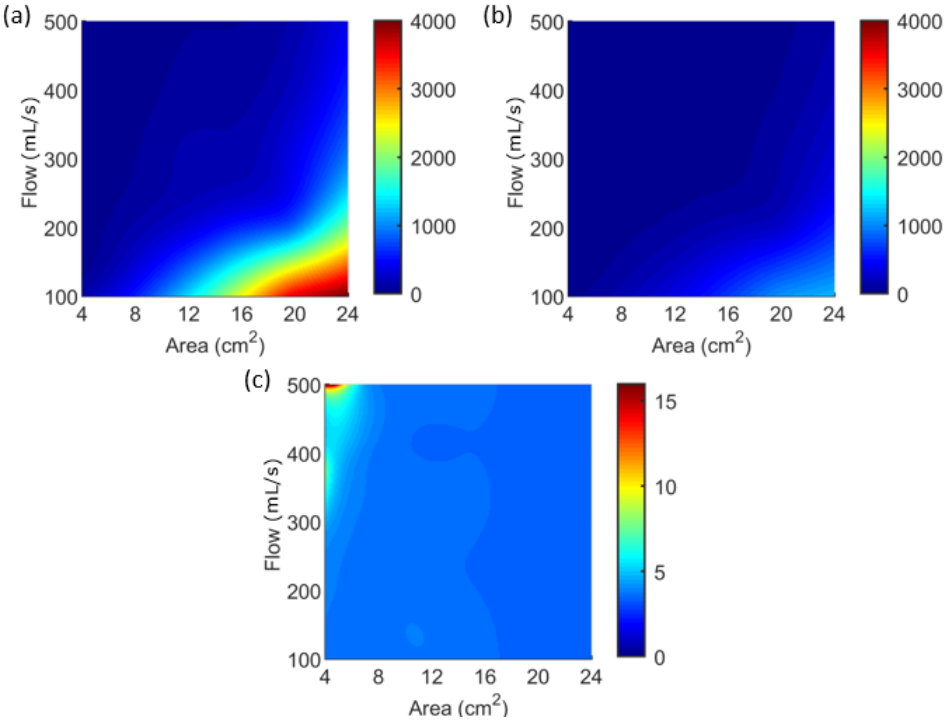

Figure 7. (**a**) Resulting $\gamma|_{Ao}$ trend as a function of flow and area; (**b**) Resulting $\gamma|_{PA}$ trend as a function of flow and area; (**c**) Trend of the ratio $\gamma|_{Ao} : \gamma|_{PA}$ to changes in flow and area.

3.2. Results from the Application of the Image-Based Method

The results related to the application of the χ-method on the in silico models are reported here.

The FSI simulations of both models M_1 and M_2 for all the different stiffnesses assigned to the vessel wall achieved solution convergence. An example of flow and area variations (for E = 1.7 MPa), as extracted from the slices S perpendicular to the model's center lines, are reported in Figure 8.

Negligible variations among sections were found for the M_1 case, for both flow and area waveforms, according to the regular shape of the model, assuring the conservation of the investigated quantities (Figure 8a,b). However, the flow and area trends at the sections from M_2 showed significant differences, due to either flow partition through supra-aortic branches (Figure 8c) or lumen reduction in the center line of the vessel (Figure 8d).

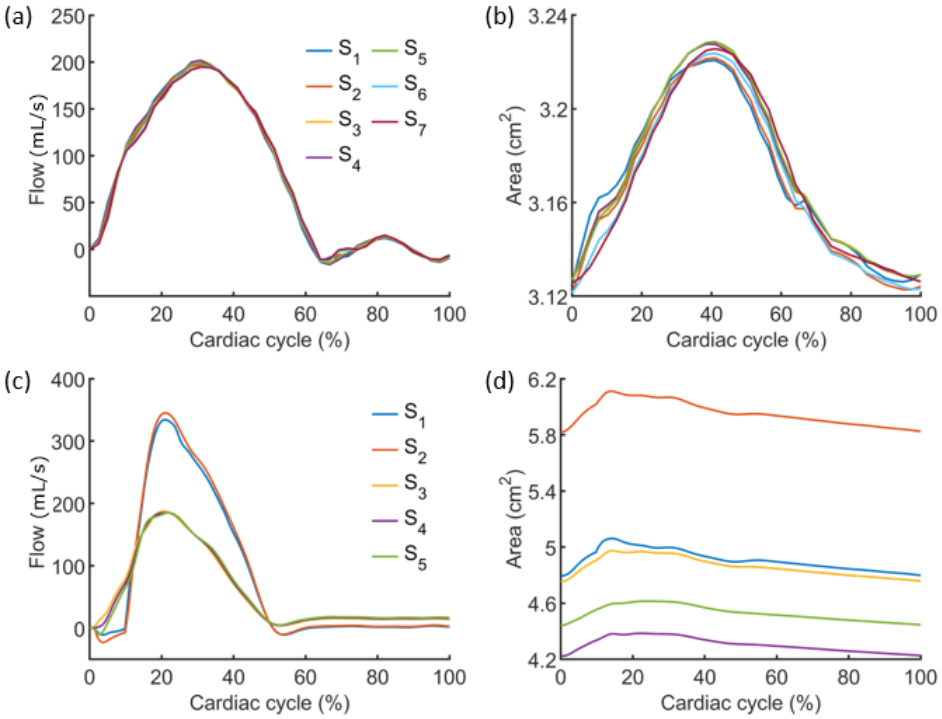

Figure 8. Flow (left panel) and area (right panel) variations along the cardiac cycles for all the selected sections S for the U-shaped model M_1 (**a**,**b**) and the patient-specific aortic model M_2 (**c**,**d**), referred to the simulation with E = 1.7 MPa.

Generally, the flow was found to preserve the same trend among the different tested E values, while the area changed accordingly, i.e., increasing for softer walls and reducing for higher stiffnesses. Figure 9 shows the coupling of flow and area information, namely the QA loop, together with the points considered for linear interpolation for the PWV estimation. The reported example plots are referred to the S_3 of both models, for E = 1.7 MPa. QA loops changed according to the area variations due to the E of the vessel wall.

Given one of the eight FSI simulations run, the PWV was computed for each slice S from the related QA loop, together with A_S^d and Q_S^p. Therefore, γ was obtained according to the $\gamma|_{Ao}$ function, using Equation (13). E_{PWV} and E_χ values were calculated and compared to the ground truth represented by the E values assigned to the vessel wall of the two models.

The comparative results are summarized in Figure 10, showing the percentage differences between the estimated (E_{PWV} and E_χ) and the assigned E value for M_1 and M_2 models, at each specific slice.

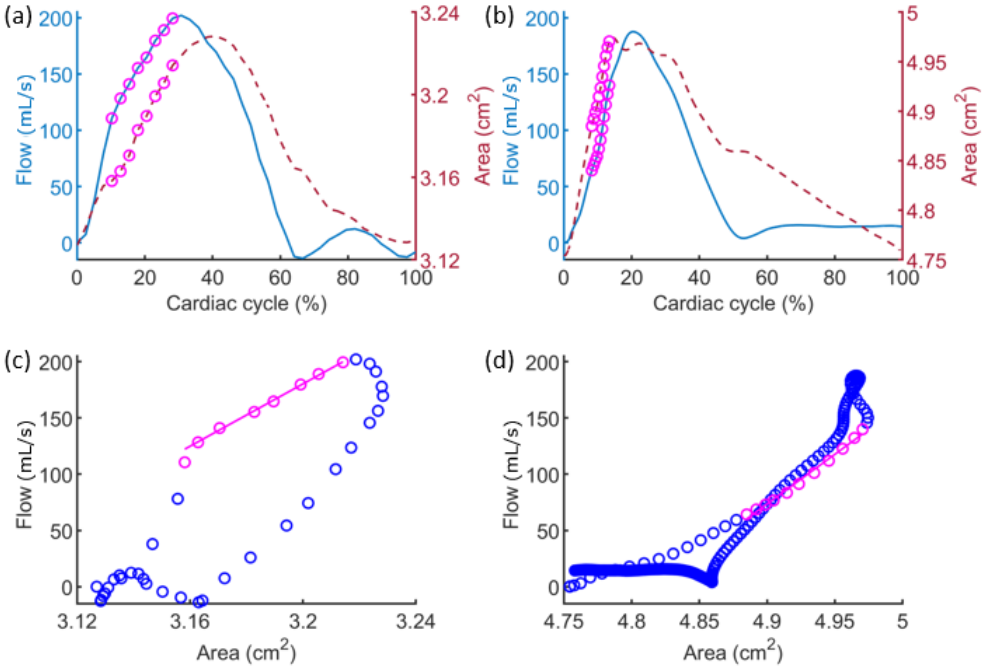

Figure 9. Flow (blue solid line) and area (red dashed line) variations with highlighted points considered for linear fitting (magenta circles) for the U-shaped model M_1 (**a**) and the patient-specific aortic model M_2 (**b**) and corresponding QA loops in dark blue circles (**c**,**d**), referred to slice S_3 and E = 1.7 MPa.

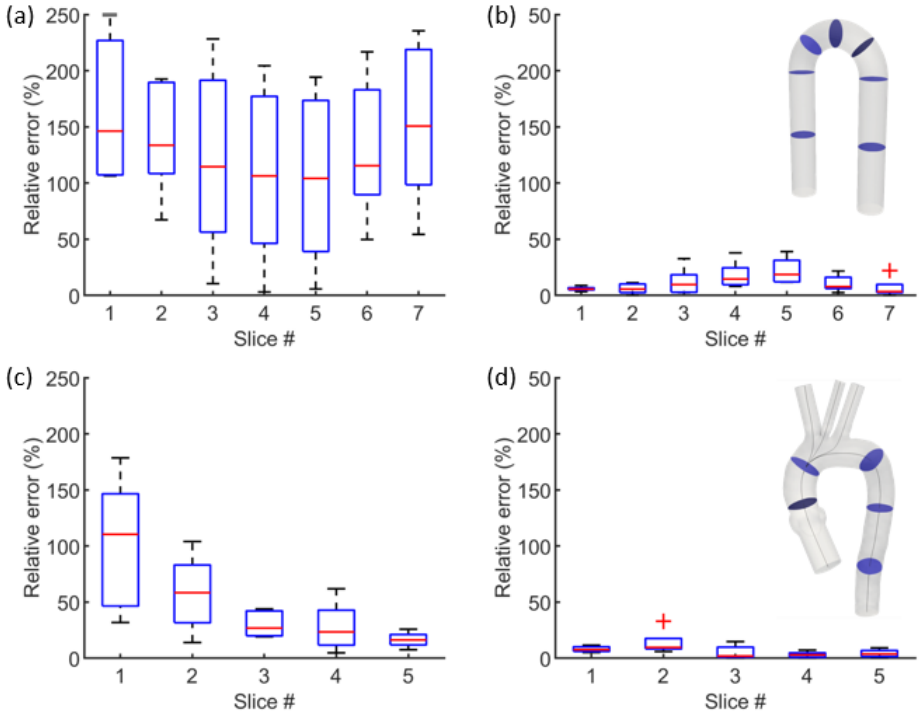

Figure 10. Percentage difference between estimated E_{PWV} and assigned E (**a**,**b**) and percentage difference between estimated E_χ and assigned E value (**c**,**d**) value at every slice for M_1 (top panel) and M_2 (bottom panel).

The overall trend was maintained for both models, with E_χ crucially reducing the gap between the stiffness wall estimation from virtual image data and the ground truth (Figure 10c,d), with an average difference of less than 10%. However, the standard E_{PWV}

prediction resulted in mean percentage errors even greater than 150%, as in the case of the S_7 section of model M_1 (Figure 10a,b).

Despite these remarkable results, a residual error was still found in the outcomes of the χ-method, with a maximum difference of 22%, for the slice S_5 of M_1 case.

4. Discussion

In this paper, we described a non-invasive methodology to extract local information of a surrogate of the Young's modulus E of the vessel wall, potentially ready-to-use in numerical simulations of vascular interventions, from solely MRI-based data, commonly acquired in routine clinical assessment of patients undergoing minimally invasive cardiovascular procedures.

The presented method is based on the PWV, which is a clinically relevant marker of arterial stiffness, strongly correlated with vascular status in aging and disease [44]. The PWV represents the portion of vessel traveled by the systolic wave in the time unit, and is commonly computed in clinical practice with the direct transit-time method [45]. Aside from invasive pressure measurements, the velocity encoded MRI modality is the only technique able to provide an estimation of PWV non-invasively, with the same accuracy as catheter-based recordings [46].

However, although several MRI-based approaches have been proposed to establish in vivo vascular material properties from PWV [25,26,47], the effective mechanical estimation is still bounded to the coupling of image-based information with invasive pressure data, thus limiting their practical usage.

Among MRI-based methods, an indirect measurement technique of local PWV, namely the QA method, was proposed by Vulliémoz et al. [35], based on the acquisition of a single-slice bi-dimensional phase contrast MRI. The main advantage of the QA method is the estimation of PWV without requiring any invasive pressure measurements. Hence, Equation (1) can provide reliable local information on vessel stiffness by considering variation in the flow with respect to the lumen deformation, measured from phase contrast image data.

However, PWV is a measure of velocity, describing the speed at which the systolic pulse propagates along a specific segment of the vessel. This makes the PWV unsuitable to describe a proper material parameter such as the Young's modulus in an isotropic linear elastic model.

For this reason, an alternative strategy was initially attempted exploiting the available formulation using the PWV and other geometric parameters to infer the module E (Equation (5)). However, this expression was found to be related to the stiffness wall but was still not fully descriptive of its proper Young's modulus, as demonstrated in the preliminary work available at [33].

In particular, the inclusion of a specific corrective factor, namely χ, is crucial to enhance the formula capability of estimating a reliable local E value of a vessel wall, referred to a specific vessel cross-section.

The χ factor was assumed to be a function of the relative area change RAC and a parameter, γ. First, the RAC value included in the formula additional information about the dynamic variation of the area along the cardiac cycle, which is otherwise not present in the standard Equation (5). Second, the γ parameter was the unknown variable, whose preliminary definition was given by assuming a dependence on the dimensions of the vessel lumen in diastole (A^d), the peak of the flow passing trough the section (Q^p) and the inner pressure range (P).

The problem was solved in two main scenarios, considering the pressure ranges of the two main large vessels, i.e., the aorta and the pulmonary artery. The γ function was then defined according to these two pressure conditions (Equation (10)).

Following the initial hypotheses, a massive in silico campaign was carried out by varying in simplified FSI vessel models the caliber (A^d) and the maximum of the inflow boundary condition (Q^p), at each pressure condition (P_{Ao} and P_{PA}), according to Figure 2.

Moreover, for each model characterized by a cross-sectional area A^d, an inlet flow condition with a maximum at Q^p and a specific outflow pressure (P_{Ao} or P_{PA}), five different stiffness values were assigned to the vessel wall (E^w), as listed in Table 1.

The huge amount of simulations were managed using a custom Python pipeline, programmed to automatically handle the entire workflow, composed of simple but time-consuming steps.

The first of the main results was the definition of the two γ functions, one for the P_{Ao} condition and the other for the P_{PA} condition. Generally, this two-variable function was found to increase with vessel dimensions and to decrease with flow rate (Figure 7). Although $\gamma|_{Ao}$ and $\gamma|_{PA}$ resulted in different ranges, as expected, their ratio was quite constant, with some significant peaks in regions related to unrealistic vascular conditions. Hence, the complete Equation (8), inclusive of the corrective factor including the γ function, was tested on "virtual" image data extracted by specific FSI models.

In the computational cases, the increased effectiveness of the Equation (8), with respect to the standard Equation (5), in the prediction of the E value was amply demonstrated. The application of the χ-method on the simulated image data resulted in an average divergence from the reference E values of 9.3%. However, an error of 89.6% was found from the adoption of the original formulation with no correction factor (Equation (5)). These first tests provided strong evidence of the necessity of modifying the standard PWV-based method to obtain a reliable estimate of the E value of the vessel wall, remarkably achieved by Equation (8).

A proper transition from the PWV information to a completely reliable E estimation of the vessel wall is still some way away, requiring further investigation. Additional simulations could be conducted to either increment the amount of γ points for the interpolation or increase the number of variables. Second, numerical models can be further exploited to produce knowledge and to highlight strategies to increase the value of the method outcomes.

In addition, the effect of uncertainties plays an important role in this context, and the implementation of stochastic analyses is crucial to assess the limitations present in the methodology. Among the image-related uncertainties, the wall thickness value, which is required to determine the $WCSA$ (Equation (4)) as part of the χ-method, is challenging to detect from imaging, due to low image resolution and a partial volume effect. In this regard, uncertainty quantification techniques [12,16] represent a valuable strategy to quantify the effect of the thickness error on the final outcome.

To provide a reliable image-based technique, in vitro models will be developed for validation purposes, using 3D-printing techniques for the fabrication of different vascular models with different deformable materials, whose mechanical properties, assessed via tensile tests, represent the ground truth. These experiments would allow the testing of the χ-method workflow in several conditions, using different phantom shapes and materials, under reliable and reproducible physiological and/or pathological conditions during the MRI acquisition phase. Doppler ultrasound represents another valuable image technique which is worth investigating, providing information on flow and vessel deformation along the cardiac cycle [48].

Such studies in the future would enhance the confidence of the predictive results provided by the proposed image-based methodology, thus favoring its application for the acquisition of in vivo patient-specific imaging data, as routinely acquired in clinics.

With respect to limitations of the study, the method presented in this study was calibrated to provide an estimation of the Young's modulus, modeling the vessel wall as an isotropic linear elastic material, thus neglecting the established hyperelastic and anisotropic properties of vascular tissues [18,49,50]. The E value computed from the χ-method is referred not only to a specific section of the vessel, providing local information on the wall stiffness, but also to the environment surrounding the vessel of interest, i.e., other vascular structures and anatomical constraints. Hence, despite considering the simplest mechanical model, the extracted E value is comprehensive of the particular and overall

context in which the patient-specific vessel occurs. The possibility of estimating, in a non-invasive and direct way, the elastic properties of a vessel in its in vivo environment would represent crucial information for patient-specific numerical modeling. The results from simulations of cardiovascular interventions would benefit from the implementation of a more reliable mechanical interaction between the implanted device and the patient-specific implantation site, which would correspond to the overall in vivo scenario of the patient's vessel of interest.

The long-term objectives of the research will include evolution from the isotropic linear elastic material to more complex models, since the workflow presented here was based on an iterative definition of unknown parameters from a series of numerical simulations. These can be applied for the extrapolation of additional mechanical parameters, taking into account the viscoelastic, hyperelastic and anisotropic features typical of vessels, in order, in the future, to provide as accurate as possible a depiction of the in vivo patient-specific mechanical properties of vascular structures in their biological environment.

Succeeding in developing a fully reliable image-based framework able to characterize the mechanical behaviour of a patient-specific vessel, directly and non-invasively, will help enhance both device design and clinical decisions towards personalised care solutions using new modelling environments for predictive, individualised healthcare to guarantee better patient safety and enhanced efficacy.

Author Contributions: Conceptualization, B.M.F. and S.C.; methodology, B.M.F. and S.C.; software, B.M.F.; validation, A.P. and G.S.; formal analysis, B.M.F. and S.C.; investigation, B.M.F.; resources, A.P. and G.S.; data curation, A.P. and B.M.F.; writing—original draft preparation, B.M.F. and S.C.; writing—review and editing, B.M.F. and S.C.; visualization, B.M.F. and S.C.; supervision, S.C.; project administration, B.M.F. and S.C.; funding acquisition, B.M.F. All authors have read and agreed to the published version of the manuscript.

Funding: This research was funded by the Italian Ministry of Health with the project IMeC (In-vivo Mechanical Characterization), grant number SG-2019-12370350.

Institutional Review Board Statement: The study was conducted in accordance with the Declaration of Helsinki, and approved by the review board of "Comitato Etico Regionale per la Sperimentazione Clinica della Toscana-sezione AREA VASTA NORD OVEST" (protocol code 18546, date of approval 5 November 2020).

Informed Consent Statement: Written informed consent has been obtained from the patient whose images were used in this study.

Conflicts of Interest: The authors declare no conflict of interest.

References

1. Capellini, K.; Gasparotti, E.; Cella, U.; Costa, E.; Fanni, B.M.; Groth, C.; Porziani, S.; Biancolini, M.E.; Celi, S. A novel formulation for the study of the ascending aortic fluid dynamics with in vivo data. *Med. Eng. Phys.* **2020**, *91*, 68–78. [CrossRef] [PubMed]
2. Zhao, S.; Wu, W.; Samant, S.; Khan, B.; Kassab, G.S.; Watanabe, Y.; Murasato, Y.; Sharzehee, M.; Makadia, J.; Zolty, D.; et al. Patient-specific computational simulation of coronary artery bifurcation stenting. *Sci. Rep.* **2021**, *11*, 16486. [CrossRef] [PubMed]
3. Miller, R.; Kerfoot, E.; Mauger, C.; Ismail, T.F.; Young, A.A.; Nordsletten, D.A. An Implementation of Patient-Specific Biventricular Mechanics Simulations With a Deep Learning and Computational Pipeline. *Front. Physiol.* **2021**, *12*, 716597. [CrossRef] [PubMed]
4. Viceconti, M.; Pappalardo, F.; Rodriguez, B.; Horner, M.; Bischoff, J.; Musuamba Tshinanu, F. In silico trials: Verification, validation and uncertainty quantification of predictive models used in the regulatory evaluation of biomedical products. *Methods* **2021**, *185*, 120–127. [CrossRef] [PubMed]
5. Antonini, L.; Mandelli, L.; Berti, F.; Pennati, G.; Petrini, L. Validation of the computational model of a coronary stent: A fundamental step towards in silico trials. *J. Mech. Behav. Biomed. Mater.* **2021**, *122*, 104644. [CrossRef] [PubMed]
6. Huberts, W.; Heinen, S.G.H.; Zonnebeld, N.; van den Heuvel, D.A.F.; de Vries, J.P.M.; Tordoir, J.H.M.; Hose, D.R.; Delhaas, T.; van de Vosse, F.N. What is needed to make cardiovascular models suitable for clinical decision support? A viewpoint paper. *J. Comput. Sci.* **2018**, *24*, 68–84. [CrossRef]
7. Gray, R.A.; Pathmanathan, P. Patient-Specific Cardiovascular Computational Modeling: Diversity of Personalization and Challenges. *J. Cardiovasc. Transl. Res.* **2018**, *11*, 80–88. [CrossRef]
8. Spronck, B.; Humphrey, J.D. Arterial Stiffness: Different Metrics, Different Meanings. *J. Biomech. Eng.* **2019**, *141*, 091004. [CrossRef]

9. Brault, A.; Dumas, L.; Lucor, D. Uncertainty quantification of inflow boundary condition and proximal arterial stiffness-coupled effect on pulse wave propagation in a vascular network: UQ of pulse wave propagation in a vascular network. *Int. J. Numer. Methods Biomed. Eng.* **2017**, *33*, e2859. [CrossRef]
10. Rego, B.V.; Weiss, D.; Bersi, M.R.; Humphrey, J.D. Uncertainty quantification in subject-specific estimation of local vessel mechanical properties. *Int. J. Numer. Methods Biomed. Eng.* **2021**, *37*, e3535. [CrossRef]
11. Romarowski, R.M.; Lefieux, A.; Morganti, S.; Veneziani, A.; Auricchio, F. Patient-specific CFD modelling in the thoracic aorta with PC-MRI–based boundary conditions: A least-square three-element Windkessel approach. *Int. J. Numer. Methods Biomed. Eng.* **2018**, *34*, e3134. [CrossRef] [PubMed]
12. Antonuccio, M.N.; Mariotti, A.; Fanni, B.M.; Capellini, K.; Capelli, C.; Sauvage, E.; Celi, S. Effects of Uncertainty of Outlet Boundary Conditions in a Patient-Specific Case of Aortic Coarctation. *Ann. Biomed. Eng.* **2021**, *49*, 3494–3507. [CrossRef] [PubMed]
13. Swanson, L.; Owen, B.; Keshmiri, A.; Deyranlou, A.; Aldersley, T.; Lawrenson, J.; Human, P.; De Decker, R.; Fourie, B.; Comitis, G.; et al. A Patient-Specific CFD Pipeline Using Doppler Echocardiography for Application in Coarctation of the Aorta in a Limited Resource Clinical Context. *Front. Bioeng. Biotechnol.* **2020**, *8*, 409. [CrossRef] [PubMed]
14. Subramaniam, D.R.; Gutmark, E.; Andersen, N.; Nielsen, D.; Mortensen, K.; Gravholt, C.; Backeljauw, P.; Gutmark-Little, I. Influence of Material Model and Aortic Root Motion in Finite Element Analysis of Two Exemplary Cases of Proximal Aortic Dissection. *J. Biomech. Eng.* **2021**, *143*, 014504. [CrossRef] [PubMed]
15. Celi, S.; Berti, S. Biomechanics and FE Modelling of Aneurysm: Review and Advances in Computational Models. In *Aneurysm*; InTech: London, UK, 2012. [CrossRef]
16. Boccadifuoco, A.; Mariotti, A.; Capellini, K.; Celi, S.; Salvetti, M.V. Validation of numerical simulations of thoracic aorta hemodynamics: comparison with in vivo measurements and stochastic sensitivity analysis. *Cardiovasc. Eng. Technol.* **2018**, *9*, 688–706. [CrossRef]
17. De Nisco, G.; Tasso, P.; Calò, K.; Mazzi, V.; Gallo, D.; Condemi, F.; Farzaneh, S.; Avril, S.; Morbiducci, U. Deciphering ascending thoracic aortic aneurysm hemodynamics in relation to biomechanical properties. *Med. Eng. Phys.* **2020**, *82*, 119–129. [CrossRef]
18. Vignali, E.; Gasparotti, E.; Celi, S.; Avril, S. Fully-Coupled FSI Computational Analyses in the Ascending Thoracic Aorta Using Patient-Specific Conditions and Anisotropic Material Properties. *Front. Physiol.* **2021**, *12*, 732561. [CrossRef]
19. Vignali, E.; Gasparotti, E.; Capellini, K.; Fanni, B.M.; Landini, L.; Positano, V.; Celi, S. Modeling biomechanical interaction between soft tissue and soft robotic instruments: Importance of constitutive anisotropic hyperelastic formulations. *Int. J. Robot. Res.* **2021**, *40*, 224–235. [CrossRef]
20. Cebull, H.L.; Rayz, V.L.; Goergen, C.J. Recent Advances in Biomechanical Characterization of Thoracic Aortic Aneurysms. *Front. Cardiovasc. Med.* **2020**, *7*, 75. [CrossRef]
21. Vignali, E.; di Bartolo, F.; Gasparotti, E.; Malacarne, A.; Concistré, G.; Chiaramonti, F.; Murzi, M.; Positano, V.; Landini, L.; Celi, S. Correlation between micro and macrostructural biaxial behavior of ascending thoracic aneurysm: A novel experimental technique. *Med. Eng. Phys.* **2020**, *86*, 78–85. [CrossRef]
22. Liu, M.; Liang, L.; Sulejmani, F.; Lou, X.; Iannucci, G.; Chen, E.; Leshnower, B.; Sun, W. Identification of in vivo nonlinear anisotropic mechanical properties of ascending thoracic aortic aneurysm from patient-specific CT scans. *Sci. Rep.* **2019**, *9*, 12983. [CrossRef] [PubMed]
23. Flamini, V.; Creane, A.P.; Kerskens, C.M.; Lally, C. Imaging and finite element analysis: A methodology for non-invasive characterization of aortic tissue. *Med. Eng. Phys.* **2015**, *37*, 48–54. [CrossRef] [PubMed]
24. Wittek, A.; Derwich, W.; Karatolios, K.; Fritzen, C.P.; Vogt, S.; Schmitz-Rixen, T.; Blase, C. A finite element updating approach for identification of the anisotropic hyperelastic properties of normal and diseased aortic walls from 4D ultrasound strain imaging. *J. Mech. Behav. Biomed. Mater.* **2016**, *58*, 122–138. [CrossRef] [PubMed]
25. D'Souza, G.A.; Taylor, M.D.; Banerjee, R.K. Evaluation of pulmonary artery wall properties in congenital heart disease patients using cardiac magnetic resonance. *Prog. Pediatr. Cardiol.* **2017**, *47*, 49–57. [CrossRef]
26. Zambrano, B.A.; McLean, N.A.; Zhao, X.; Tan, J.; Zhong, L.; Figueroa, C.A.; Lee, L.C.; Baek, S. Image-based computational assessment of vascular wall mechanics and hemodynamics in pulmonary arterial hypertension patients. *J. Biomech.* **2018**, *68*, 84–92. [CrossRef] [PubMed]
27. Sigrist, R.M.; Liau, J.; Kaffas, A.E.; Chammas, M.C.; Willmann, J.K. Ultrasound Elastography: Review of Techniques and Clinical Applications. *Theranostics* **2017**, *7*, 1303–1329. [CrossRef] [PubMed]
28. Mahmood, B.; Ewertsen, C.; Carlsen, J.; Nielsen, M. Ultrasound Vascular Elastography as a Tool for Assessing Atherosclerotic Plaques – A Systematic Literature Review. *Ultrasound Int. Open* **2016**, *2*, E106–E112. [CrossRef]
29. Low, G. General review of magnetic resonance elastography. *World J. Radiol.* **2016**, *8*, 59. [CrossRef]
30. Pruijssen, J.T.; de Korte, C.L.; Voss, I.; Hansen, H.H.G. Vascular Shear Wave Elastography in Atherosclerotic Arteries: A Systematic Review. *Ultrasound Med. Biol.* **2020**, *46*, 2145–2163. [CrossRef]
31. Huang, C.; Lan, Y.; Xu, G.; Zhai, X.; Wu, J.; Lin, F.; Zeng, N.; Hong, Q.; Ng, E.Y.K.; Peng, Y.; et al. A Deep Segmentation Network of Multi-Scale Feature Fusion Based on Attention Mechanism for IVOCT Lumen Contour. *IEEE/ACM Trans. Comput. Biol. Bioinform.* **2021**, *18*, 62–69. [CrossRef]
32. Celi, S.; Gasparotti, E.; Capellini, K.; Vignali, E.; Fanni, B.M.; Ait-Ali, L.; Cantinotti, M.; Murzi, M.; Berti, S.; Santoro, G.; et al. 3D Printing in Modern Cardiology. *Curr. Pharm. Des.* **2021**, *27*, 1918–1930. [CrossRef] [PubMed]

33. Fanni, B.M.; Sauvage, E.; Celi, S.; Norman, W.; Vignali, E.; Landini, L.; Schievano, S.; Positano, V.; Capelli, C. A Proof of Concept of a Non-Invasive Image-Based Material Characterization Method for Enhanced Patient-Specific Computational Modeling. *Cardiovasc. Eng. Technol.* **2020**, *11*, 532–543. [CrossRef] [PubMed]
34. Milan, A.; Zocaro, G.; Leone, D.; Tosello, F.; Buraioli, I.; Schiavone, D.; Veglio, F. Current assessment of pulse wave velocity: Comprehensive review of validation studies. *J. Hypertens.* **2019**, *37*, 1547–1557. [CrossRef] [PubMed]
35. Vulliémoz, S.; Stergiopulos, N.; Meuli, R. Estimation of local aortic elastic properties with MRI: Estimation of Local Aortic Elastic Properties. *Magn. Reson. Med.* **2002**, *47*, 649–654. [CrossRef]
36. Rabben, S.I.; Stergiopulos, N.; Hellevik, L.R.; Smiseth, O.A.; Slørdahl, S.; Urheim, S.; Angelsen, B. An ultrasound-based method for determining pulse wave velocity in superficial arteries. *J. Biomech.* **2004**, *37*, 1615–1622. [CrossRef]
37. Boonyasirinant, T.; Rajiah, P.; Flamm, S.D. Abnormal aortic stiffness in patients with bicuspid aortic valve: phenotypic variation determined by magnetic resonance imaging. *Int. J. Cardiovasc. Imaging* **2019**, *35*, 133–141. [CrossRef]
38. Tiwari, K.K.; Bevilacqua, S.; Aquaro, G.; Festa, P.; Ait-Ali, L.; Solinas, M. Evaluation of Distensibility and Stiffness of Ascending Aortic Aneurysm using Magnetic Resonance Imaging. *J. Nepal Med. Assoc.* **2016**, *55*, 67–71. [CrossRef]
39. Sugawara, J.; Tomoto, T.; Tanaka, H. Heart-to-Brachium Pulse Wave Velocity as a Measure of Proximal Aortic Stiffness: MRI and Longitudinal Studies. *Am. J. Hypertens.* **2019**, *32*, 146–154. [CrossRef]
40. Bramwell, J.C.; Hill, A.V. The velocity of pulse wave in man. *Proc. R. Soc. London. Ser. B Contain. Pap. Biol. Character* **1922**, *93*, 298–306. [CrossRef]
41. Laurent, S.; Cockcroft, J.; Van Bortel, L.; Boutouyrie, P.; Giannattasio, C.; Hayoz, D.; Pannier, B.; Vlachopoulos, C.; Wilkinson, I.; Struijker-Boudier, H.; et al. Expert consensus document on arterial stiffness: Methodological issues and clinical applications. *Eur. Heart J.* **2006**, *27*, 2588–2605. [CrossRef]
42. Ahrens, J.; Geveci, B.; Law, C., ParaView: An End-User Tool for Large-Data Visualization. In *Visualization Handbook*; Elsevier: Amsterdam, The Netherlands, 2005; pp. 717–731. [CrossRef]
43. Westerhof, N.; Lankhaar, J.; Westerhof, B.E. The arterial Windkessel. *Med. Biol. Eng. Comput.* **2009**, *47*, 131–141. [CrossRef] [PubMed]
44. Vatner, S.F.; Zhang, J.; Vyzas, C.; Mishra, K.; Graham, R.M.; Vatner, D.E. Vascular Stiffness in Aging and Disease. *Front. Physiol.* **2021**, *12*, 762437. [CrossRef] [PubMed]
45. Segers, P.; Rietzschel, E.R.; Chirinos, J.A. How to Measure Arterial Stiffness in Humans. *Arterioscler. Thromb. Vasc. Biol.* **2020**, *40*, 1034–1043. [CrossRef]
46. Grotenhuis, H.B.; Westenberg, J.J.M.; Steendijk, P.; van der Geest, R.J.; Ottenkamp, J.; Bax, J.J.; Jukema, J.W.; de Roos, A. Validation and reproducibility of aortic pulse wave velocity as assessed with velocity-encoded MRI. *J. Magn. Reson. Imaging* **2009**, *30*, 521–526. [CrossRef] [PubMed]
47. Bertoglio, C.; Barber, D.; Gaddum, N.; Valverde, I.; Rutten, M.; Beerbaum, P.; Moireau, P.; Hose, R.; Gerbeau, J.F. Identification of artery wall stiffness: In vitro validation and in vivo results of a data assimilation procedure applied to a 3D fluid–structure interaction model. *J. Biomech.* **2014**, *47*, 1027–1034. [CrossRef]
48. Wang, Z.; Yang, Y.; Yuan, L.j.; Liu, J.; Duan, Y.y.; Cao, T.s. Noninvasive Method for Measuring Local Pulse Wave Velocity by Dual Pulse Wave Doppler: In Vitro and In Vivo Studies. *PLoS ONE* **2015**, *10*, e0120482. [CrossRef]
49. Chen, Z.W.; Joli, P.; Feng, Z.Q. Anisotropic hyperelastic behavior of soft biological tissues. *Comput. Methods Biomech. Biomed. Eng.* **2015**, *18*, 1436–1444. [CrossRef]
50. Nolan, D.R.; Gower, A.L.; Destrade, M.; Ogden, R.W.; McGarry, J.P. A robust anisotropic hyperelastic formulation for the modelling of soft tissue. *J. Mech. Behav. Biomed. Mater.* **2014**, *39*, 48–60. [CrossRef]